Effect of Microwave Annealing on Low Energy ion implanted wafer

by

Zhao Zhao

A Thesis Presented in Partial Fulfillment
of the Requirements for the Degree
Master of Science

Approved July 2013 by the
Graduate Supervisory Committee:

Terry Alford, Chair
David Theodore
Stephen Krause

ARIZONA STATE UNIVERSITY

August 2013

ABSTRACT

Rapid processing and reduced end-of-range diffusion effects demonstrate that susceptor-assisted microwave annealing is an efficient processing alternative for electrically activating dopants and removing ion-implantation damage in ion-implanted semiconductors. Sheet resistance and Hall measurements provide evidence of electrical activation. Raman spectroscopy and ion channeling analysis monitor the extent of ion implantation damage and recrystallization. The presence of damage and defects in ion implanted silicon, and the reduction of the defects as a result of annealing, is observed by Rutherford backscattering spectrometry, moreover, the boron implanted silicon is further investigated by cross-section transmission electron microscopy. When annealing B^+ implanted silicon, the dissolution of small extended defects and growth of large extended defects result in reduced crystalline quality that hinders the electrical activation process. Compared to B^+ implanted silicon, phosphorus implanted samples experience more effective activation and achieve better crystalline quality. Comparison of end-of-range dopants diffusion resulting from microwave annealing and rapid thermal annealing (RTA) is done using secondary ion mass spectroscopy. Results from microwave annealed P^+ implanted samples show that almost no diffusion occurs during time periods required for complete dopant activation and silicon recrystallization. The relative contributions to heating of the sample, by a SiC susceptor, and by Si self-heating in the microwave anneal, were also investigated. At first 20s, the main contributor to the sample's temperature rise is Si self-heating by microwave absorption.

ACKNOWLEDGMENTS

I would like to gratefully thank my advisor Dr. Terry Alford for letting me join this group and giving me so much instructions and inspiration. I gain not only knowledge but also motivation after talking with him. I would also thank Rajitha Vemuri for her support and generous help on experiments and measurements. She leads me to get into this project and helps me to start.

I would also express my gratitude to my committee, Dr. David Theodore and Dr. Stephen Krause, for their time and suggestions.

I would like to thank Dr. David Theodore in Freescale for his great help on electron microscopy measurement and his kindness to provide suggestion to data analysis. I would like to thank Dr. Benjamin French in Intel for SIMS measurement and analysis. His extremely helpful suggestions on SIMS analysis help me to get the reasonable data. I would like to thank Barry Wilkens, Jason Ng, Wei Lu and Dr. S.S. Lau for their help in material characterization, sample preparation and data measurement; Sayantan Das and Aritra Dhar for their kind suggestions.

Finally, I would owe my work to my parents, and thank for their support and love. Without them, I would not be here and accomplish this thesis.

TABLE OF CONTENTS

Page

LIST OF TABLES ... v

LIST OF FIGURES ... vi

CHAPTER

1 Introduction ... 1

1.1 Ion implantation ... 1

1.2 Energy loss process in ion implantation ... 2

1.3 Post-implantation Annealing ... 3

1.4 Motivations ... 4

1.5 Microwave annealing technology ... 5

1.6 Dielectric properties ... 6

1.7 Volumetric heating ... 8

1.8 SiC susceptor ... 9

2 Experiment ... 10

2.1 Experiment setup ... 10

2.2 Sample preparation ... 10

2.3 Characterization ... 11

2.3.1 Sheet resistance measurement ... 12

2.3.2 Hall Measurement ... 13

CHAPTER Page

2.3.3 Raman Spectroscopy 16

2.3.4 Rutherford Backscattering Spectrometry 17

2.3.5 Cross-section Transmission Electron Microscope 19

2.3.6 Secondary Ion Mass Spectroscopy 20

3 Results and discussion on the electrical and structural properties 22

3.1 Heating curves 22

3.2 Dopants electrical activation 23

3.3 Recrystallization and defects evolution 25

3.3.1 Raman Spectra 25

3.3.2 RBS/ion channeling spectra 28

3.3.3 TEM images 30

3.3.4 SIMS profiles 32

4 Discussion on the heating behavior 36

5 Summary and Conclusion 39

6 Further work 40

REFERENCES 41

LIST OF TABLES

Table Page

1. Hall Measurement Results 24

2. Annealing condictions and the corresponding sheet resistance.............................34

LIST OF FIGURES

Figure Page

1. The variation of ε' and ε" with frequency for water 7

2. The dielectric loss factor as a function of microwave absorption 9

3. Experiment setup. 10

4. Schematic of a typical in line four-point probe setup. 13

5. Schematic of Hall measurement mechanism. 144

6. Configuration for van der Pauw Hall measurements 15

7. Raman Spectrometer 17

8. Rutherford backscattering Spectrometry Instrumentation System 18

9. Schemitic of the working principle of SIMS 20

10. Temperature as a function of time for ion implanted Si wafers 22

11. Rsh as function of time for ion implanted Si wafers 24

12. Raman Spectra for ion implanted Si wafers 27

13 RBS spectra of ion implanted Si wafers. 29

14. TEM image of boron implanted Si. 31

15. SIMS profile for ion implanted Si prior and after annealing 33

16. Temperature vs.time for susceptor alone and Si on susceptor. 37

1 Introduction

The revolution of technology is powered by creation and fast development of integrated circuits. The first electrical computer ENIAC which weighed 30 tons, took up1800 square feet and was used only in laboratory in 1946, while the recent ultrabook laptop has a thickness of less than 25mm. This huge progress is the best evidence of Moore's law which predicts the number of transistors on the integrated circuit doubles approximately every two years. The increasing density of transistors on chips is implemented by the advanced the silicon processing technology.

The whole process of silicon processing is very complicated. First, the signal crystalline silicon ingots are cut into wafers and polished to an extremely flat and smooth surface[1]. Then, oxidization, deposition, lithography, ion implantation, etching, and planarization are done on the wafers and some of those steps are even repeated several times until the die is accomplished[1]. Each step needs to meet a strict requirement to ensure a high yield[1]. This thesis will focus on one of these steps, a post implantation annealing technique.

1.1 Ion implantation

In semiconductor industry, introducing dopants into the intrinsic semiconductor is the most common way to obtain low resistivity layers in semiconductor applications[2]. The methods of introducing dopant atoms include: diffusion and ion implantation. The most commonly used method is ion implantation in which the dopant atoms are ionized

and accelerated to 10 - 150 keV energy or higher and bombarded into the wafer. During this process, a large amount of vacancies and disordered array of atoms (*i.e.,* damages) are created in the wafer surface, leading to amorphization of the implanted layer[3].

1.2 Energy loss process in ion implantation

When dopants are implanted into the Si wafers, they travel through the material, collide with atoms and finally come to rest due to the loss of energy[2]. The loss of energy has two mechanisms: nuclear stopping and electronic stopping[4]. Depending on the implantation energy, the nuclear stopping or electronic stopping dominates and the extent of the damage varies. The higher implantation energy does not necessarily mean more damage. In nuclear energy loss, ions with low incident energy are able to interact with atomic cores of materials and lose energy in their elastic collision[4]. Ions transfer energy to atoms, resulting in eventual displacement of these atoms[4]. Hence, damage is created in this process. In electronic energy loss event, the energetic particles with high velocity lose energy primarily through inelastic collisions with electron cloud, transferring energy to electrons, resulting in little damage[4]. Based on the energy loss mechanism, if two kinds of dopants species implanted with the same energy, they may experience different energy loss because their different masses lead to different energy loss mechanism. Therefore, different dopants with same implantation energy can cause different levels of damage. It is reported that for boron, electronic energy loss dominates in the range of 10 to 1000 keV, while for arsenic and phosphorus, the electronic energy loss dominates after energies of 130 and 700 keV, respectively[4,5]. In our study, boron and phosphorus ions are

implanted with energy of 15 keV. According to the energy range of the two energy-loss mechanisms in Si for different implants[5], boron implants mainly experience electronic loss while nuclear energy loss dominates in phosphorus implanted samples, suggesting that\ phosphorus dopants cause more damage than boron dopants do.

1.3 Post-implantation Annealing

Resistivity of the wafer is still high after implantation due to the absence of long range order of the substrate lattice and the presence of dopants in off-lattice sites. Dopant activation is achieved by relocation of dopant atoms from interstitial sites, or off-lattice sites, into substitutional sites, where they can act as donors or acceptors and contribute electrons or holes. Annealing implanted Si samples is performed to promote dopant activation and to obtain conductive materials. Annealing methods to achieve solid phase epitaxial growth (SPEG) used widely are well-established techniques in industry, including, laser anneal, metal induced crystallization (MIC), rapid thermal anneal (RTA). However, laser annealing suffers from dopants diffusion and surface melting. In pulsed laser annealing, the laser energy is absorbed in the near surface region and causes the melting of surface the layer[6]. The liquid phase epitaxy is responsible for the transition from amorphous to signal crystalline silicon[7]. Even the laser annealing is able to remove all the defects in surface layer[7], the large diffusion coefficient in the liquid phase leads to the extensive dopant diffusion which weakens advantage of the laser annealing and hinders the achievement of a shallow junction. In MIC, the metal layer, such as Ag and Au, is deposited on amorphous silicon[8,9]. The metal atoms begin to intermix with the

amorphous Si layer. Then the nuclearization of c-Si occurs at the interface [8,9] and the Si crystallite is surround by metal-Si compounds. The Si atoms from the amorphous layer diffuse through the metal-Si compounds, precipitate on the crystalline phase nuclei , and cause the radial growth of crystalline Si [8,9]. Finally, the metal is segregated to the top and bottom surface of the silicon[8,9]. Compared to the direct reordering of the amorphous lattice which require a high temperature, this mechanism provides a reduced free energy for the system, so that the crystallization could be done in relative low temperature at ~250 ^{o}C[9] . However, the contamination of ultra-thin metal film will lead to the failure of the devices[10]. The RTA achieves the rapid heating rate using Quartz halogen lamps or tungsten halogen lamps, which provides radiation energy to recrystallize the amorphous layer in a short time and obtains defect free profile. However, even RTA minimizes the diffusion length by short annealing at high temperature, it still causes the end of range diffusion[11].

1.4 Motivations

Driven by the International Technology Roadmap for Semiconductors (ITRS), the device features are scaling down significantly and the corresponding junction depth keeps decreasing[12]. The low energy implantation could create a shallow junction, however, the post implantation thermal annealing will cause the dopants diffuse towards the substrate so the junction is not that shallow any more. Fortunately, it is reported that the susceptor-assisted microwave annealing achieves a high quality crystalline Si layer in a short time and successful minimizes end-of-range diffusion in the As^+ implanted Si[10]. The effect of

microwave annealing on different dopant species implanted silicon wafers is investigated in this study.

1.5 Microwave annealing technology

The interaction of microwave and materials includes absorption, transmission and reflection. However, only the absorption procedure which is caused by the energy loss in the interaction leads to the heating of materials[13]. The energy loss includes the ion conduction loss and dipole polarization loss[14].

In ion conduction loss, the free electrons move back and forth, or ions move within the lattice network under the changing electromagnetic field[11]. The moving electrons or ions collide with other species and dissipate energy, leading to generation of heat in materials[14].

The dipole polarization loss is based on polarization mechanisms. In term of electronic polarization, under the influence of an external electric field, the negatively charged electron cloud of an atom becomes displaced with respect to its positively charged core[14]. In ionic material, such as the alkali halides, cations and anions are displaced from their equilibrium positions under an external field. Moreover, many materials already possess permanent dipoles that can be aligned in an external electric field. This is called molecular polarization[15]. In dielectric materials, electric dipoles are created and align themselves with electromagnetic field. They even rotate as the field alternates. As the field frequency increases, the rotation of dipole lags behind the field.

Hence, dipoles collide with either surrounding electron cloud or other dipoles, resulting energy loss and heat generating.

Typically, losses are reported as dielectric loss ε''. The absolute value of absorption and the proportion of the ion conduction loss and dipole polarization loss are dependent on MW frequency and material parameters[15]. The ionic conduction loss dominates at low frequencies, because the time letting electrons transport in one direction reduces as the frequency increases, resulting in few collision events and less heat generation at high frequency[14]. On the other hand, dipole polarization loss is dominant at high frequencies. The lag between the rotation of dipole and changing of electromagnetic field becomes severe at high frequency so that most of the energy loss results from the friction of dipoles[14].

1.6 Dielectric properties

ε' is the dielectric constant relating the in-phase component of the electric displacement *D* to the applied electric field and ε' is proportional to the energy stored. ε'' is the loss factor relating the out phase component to the applied field[16,17].

According to the Debye equation below, ε' and ε'' not only depend on the frequency, but also depend on temperature.

$$\varepsilon' = \varepsilon_\infty + (\varepsilon_s - \varepsilon_\infty)/(1+\omega^2\tau^2) \quad (1)$$

$$\varepsilon'' = (\varepsilon_s - \varepsilon_\infty)\omega\tau/(1+\omega^2\tau^2) \quad (2)$$

where ε_s and ε_∞ are the static and high-frequency limits of ε', τ is the relaxation time which is associated with temperature, ω is the angular frequency of the filed.

When the dipoles are able to follow the changing of the applied field, the dielectric constant maintains its maximum value[18]. As the frequency increases, the dipolar polarization falls behind the field. When the frequency reaches a point where the dipole is no longer rotates significantly with respect to changing field, the effective polarization decrease[18]. The reduced effective polarization means a decrease in the dielectric constant and an increase of the loss factor as the frequency increase[18]. Figure 1.1 shows water's dielectric properties as a function of frequency.

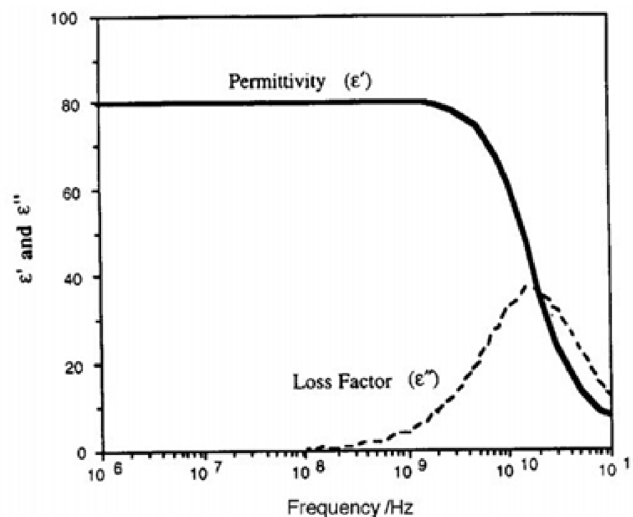

Figure 1.1 The variation of ε' and ε'' with frequency for water at 20 °C [18]

For different materials, their ε' and ε'' dependence of temperature varies. For example, water's ε'' decreases as temperature increases at a fixed frequency, while ε'' of quartz increases with temperature. Moreover, for the same material at different frequencies, the relationship between ε'' and temperature varies[18].

1.7 Volumetric heating

Microwave heating is dominated by volumetric heating mechanism. In volumetric heating, the heat energy is transferred through the surface electromagnetically, rather than flow as a heat flux[16]. The rate of heating is no longer limited by thermally diffusivity and surface temperature[16]. Hence, the uniformity of heat distribution is greatly improved[16]. The power absorbed by the dielectric per volume[18]:

$$P = \omega \varepsilon_0 \varepsilon_{eff}'' E_{rms}^2 \quad (3)$$

Where, ω is the angular microwave frequency, ε_0 is permittivity of free space, ε_{eff}'' is the relative effective dielectric factor. E_{rms} is the average electric field in dielectrics[18].

The electric field decreases as it penetrates materials, which means volumetric heating is only valid for thin layers. The penetration depth is defined as the distance from the sample surface where the absorbed power is 1/ e of the absorbed power at the surface[17].

$$D_p = \frac{c\varepsilon_0}{2\pi f \varepsilon''} \quad (4)$$

According equation (4), Materials with very high dielectric loss factor have very small penetration depths, approaching to zero. Materials with such dielectric property are treated as reflectors. Similarly, Materials with a very low dielectric loss factor have a large penetration depth. As a result, these materials are transparent to the microwave field. The materials that mid-ranged dielectric factors can absorb microwave energy effectively as Figure 1.2 shown[17].

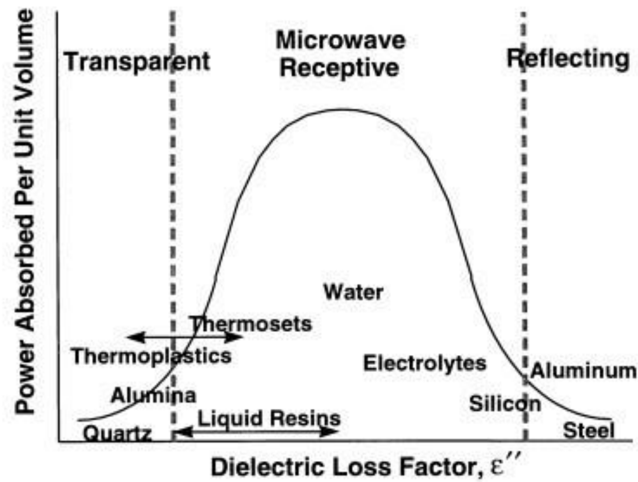

Figure 1.2 Relationship between the dielectric loss factor and ability to absorb microwave power for some common materials[17]

1.8 SiC susceptor

When the ion implanted Si is annealed at the microwave cavity, it cannot obtain a high temperature without any external heat supply[10]. To achieve a temperature that is high enough to repair the damages and activate the dopants, additional heat is required. For instance, to anneal amorphous Si wafers, susceptor-assisted microwave heating is suggested. This method is called hybrid heating since it makes use of volumetric heating of microwaves, and conductive heating of the susceptor[11]. The susceptor, made up of Al_2O_3 infused SiC, is a lossy material that can heat up by absorbing microwave radiations. The large dielectric loss factor of SiC ensures that only its surface can be heated to very high temperatures, which in turn allows the sample on the susceptor to be heated up. More importantly, due to the large heat capacity (1.09 J/mol ·K) and high thermal conductivity (350 W/m ·K) of SiC, temperature gradients across the suscepotor do not exist, which allows an excellent uniform heating[19].

2 Experiment

2.1 Experiment setup

The microwave setup is shown in Figure 2.1. The $2.8x10^4$ cm^3 cavity microwave oven used for post-implantation annealing generated a single frequency 2.45 GHz using a 1200 W magnetron source. The SiC susceptor that assisted heating samples to higher temperatures was carved to a 1.5 cm $\times$ 1.5 cm groove in the center so that a sample could be mounted on it and received uniform heating from the underneath. The surface temperature of samples as a function of time was monitored in an in-situ manner by Raytek Compact MID series pyrometer.

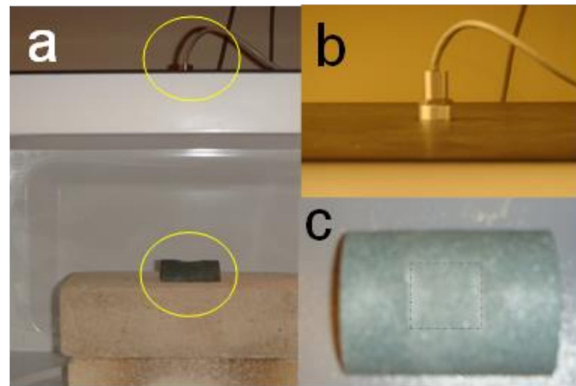

Figure 2.1 Experiment setup a) The microwave pyrometer-susceptor setup; b) pyrometer to measure in-situ temperature; c) SiC-Al susceptor with a 1.5 cm $\times$ 1.5 cm groove to mount the sample to provide uniform heating.[20]

2.2 Sample preparation

The n-type (001) oriented Si wafers having a resistivity range of 1-5 Ω-cm implanted with boron (acceptor) were cleaned according the Radio Corporation of

America procedure. Eaton Nova NV10-180 batch process ion implanter was used to implant the cleaned Si wafers with an energy of 15 keV and doses of $2x10^{15}$ cm^{-2}, 3 $x10^{15}$ cm^{-2}, 4 $x10^{15}$ cm^{-2}. During the implantation, the wafers were titled at 7 °off the incident beam with a 45° plane twist to minimize the ion channeling. The procedure was repeated with the same energy and doses on another set of (001) oriented Si wafers with 1-5Ω-cm p-type boron doped substrates, but phosphorus (donor) implants were used instead of boron implants.

The microwave annealing was done by mounting the samples onto a SiC susceptor that assisted in heating the samples to higher temperatures. The surface temperature of the samples was monitored as a function of time in an in-situ manner, using Raytek Compact MID series pyrometer. The emissivity of the sample was estimated by calibration of the pyrometer's temperature reading against temperature measured by a thermocouple. To cover the large temperature range in annealing, two pyrometers were used, with measurable temperature range of 0-600 ^oC and 200-1000 ^oC, respectively. The anneal time for boron implanted samples ranged 60-400 seconds and the corresponding surface temperature range was 663-747 ^oC. The anneal time for phosphorus implanted samples ranged 10-240 seconds and the corresponding surface temperature range was 294-740 ℃.

2.3 Characterization

At the evaluated temperature, the electrical and structural properties of ion implanted Si are expected to be improved. Therefore, as-implanted samples and annealed

samples were characterized by several techniques. To estimate the dopants activation, the sheet resistance (R_{sh}) of each sample with different process time was measured by 4-point probe. Hall measurement was also conducted to give the carrier concentrations as well as determine activation percentage. The extent of recrystallization was assessed by Raman spectroscopy and ion channeling using Rutherford backscattering spectrometry (RBS). The defects evolution and recrystallization was inspected by cross-section transmission electron microscope (TEM). Apart from that, the depth profile were measured by secondary ion mass spectrometry (SIMS). To compare the extent of diffusion in microwave annealing and RTA samples, SIMS is also performed on RTA treated samples.

2.3.1 Sheet resistance measurement

The typical in line four-point probe quipped with a 100mA Keithley 2700 digital multimeter is used to measure the sheet resistance. This measurement is to testify the sheet resistance drop after the samples are annealed, which is the evidence of electrical activation. The probes with a spacing of 1.016 mm is shown in Figure 2.2, in which the two outer probes measure the passing current and the two inner probes sense the voltage drop along the distance between the two inner probes. The advantage of this configuration is that the probe resistance R_p, the probe contact resistance R_{cp} and the spreading resistance R_{sp} associated with measurement are eliminated by only measuring voltage drop between the two inner probes[3]. These parasitic resistances are negligible for the two voltage probes because the voltmeter has sufficient high impedance so that a very small current passes the parasitic resistances, and the corresponding voltage drop along

those parasitic resistances could be neglected. The sheet resistance is calculated by taking the ratio of the measured voltage and the current and multiplying a correction factor.

The sheet resistance can be calculated by the following expression:

$R_s = (V/I) \text{ x } CF$ (1)

where CF is correction factor. The probe spacing, conduction/non-conducting bottom, wafer shape, wafer size and nearness to the wafer edge all affect the correction factor[3]. V/I is read from the monitor, V is the voltage drop across the material and I is the current driven through the sample.

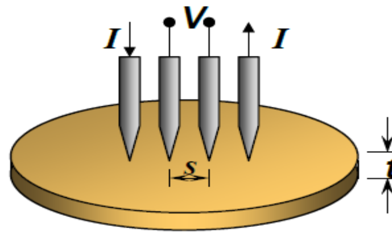

Figure 2.2 Schematic of a typical in line four-point probe setup[3].

2.3.2 Hall Measurement

Hall measurement is a widely used technique that provides electrical properties, such as, resistivity, doping type (n-type or p-type), mobility of majority carriers and sheet carrier concentration. In our study, Hall measurement was conducted using Van der Pauw method on the annealed sample to obtain accurate resistivity, the carrier concentration as well as to determine their activation percentage.

Hall measurement is based on hall effect. The current is applied on the semiconductor under the presence of a magnetic field that is perpendicular to current direction, as shown in Figure 2.3. Initially, the electrons flow in the curved path and hit

the bottom side of the sample due to Lorentz force, which is perpendicular to the direction of moving electrons and proportional to their velocity. The expression of the Lorentz force is shown as follow:

$$F_L = q.v.B \qquad (3)$$

where q is the charge on the particle, v is velocity, B is strength of magnetic field.

The electrons accumulate on the bottom side while the holes accumulate on the top side, then an electric field is created. In steady-state, the Coulomb force which is created by the electric field is in the opposite direction of Lorentz force. The two forces will exactly balance out. Hence, the electrons flow along its initial direction, in a straight line. This relationship would be expressed by the following expressions:

$$q\varepsilon = F_L = qvB \qquad (4)$$

$$I = qAnv = qwdnv \qquad (5)$$

$$V_H = w\varepsilon = wBv = \frac{IB}{qdn} \qquad (6)$$

where the ε is the strength of electrical field, A is area of cross section of the sample, w and d is height and width of the sample, n is the carrier density.

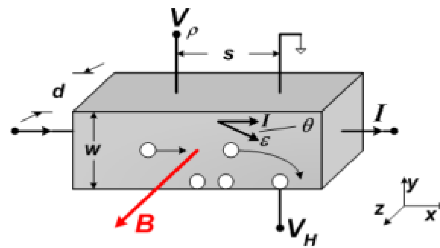

Figure 2.3 Schematic of Hall effect mechanism[3].

The hall coefficient is represented by R_H ,

$$R_H = \frac{dV_H}{BI} \qquad (7)$$

Then, the resistivity ρ, carrier density *p* or *n*, hall mobility μ_H is calculated by following equations:

$$\rho = \frac{dw}{s}\frac{V_\rho}{I} \qquad (8)$$

$$p = \frac{r}{qR_H}; n = -\frac{r}{qR_H} \qquad (9)$$

$$\mu_H = |\sigma R_H| \qquad (10)$$

Where V_ρ and *I* is the measured voltage and current.; r is Hall scattering factor; σ is the conductivity.

The current *I* and voltage V_ρ is measured by Van der Pauw method. As it is required, the sample should be symmetrical, often a square shaped sample, and thin enough. Its length and width are much larger than the thickness so that the sample could be considered as two dimension. Figure 2.4 shows the configuration of Van der Pauw method. The top left corner is numbered as 1 and the rest corners are numbered 2 to 4 in a counter-clockwise direction. The current flows through two adjacent corners, for example, 1 and 2, and the voltage is measured on the other two adjacent corners, like 3 and 4.

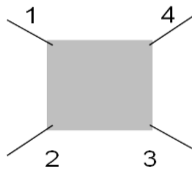

Figure 2.4 Configuration for the contacts made to perform van der Pauw Hall measurements[21].

Ohmic contacts are needed for the current and voltage measurement. However, not all the metal could form Ohmic contacts with Si wafer. In this study, indium was properly selected to form Ohmic contacts with Si wafer and was deposited on the four corners of the square sample using solder ion, then the samples were placed on printed circuit board and the contacts are connected to the printed circuit board by copper wires.

2.3.3 Raman Spectroscopy

Raman spectroscopy can provide structural, orientational and chemical information based on its sensitivity to the molecular vibration[21]. The structure of as-implanted and microwave annealed samples are examined by Raman line scan. Figure 2.5 is the setup of the Raman spectroscopy. A 532 nm argon laser beam impinges on the samples mounted under the optical microscope, through an Olympus 100×0.8 NA objective. The sample' spectrum is reflected into a Sopra 2000 2m double spectrometer by a 50% beam-splitter. The scattered laser light is blocked by a 532 nm notch filter. A Princeton CCD Camera with an energy dispersion of 60 pixels/cm disperses and collects the reflected light. Raman spectra are calibrated and converted to the intensity as a function of time[22]. In this setup, the laser beam incident on the sample with energy of only 1 mW, which is achieved by letting the 4 mW power beam go through a series of beam splitters and lower its energy. Damage is less likely to be created by such a low energy beam, so it is a non-destructive characterization technique.

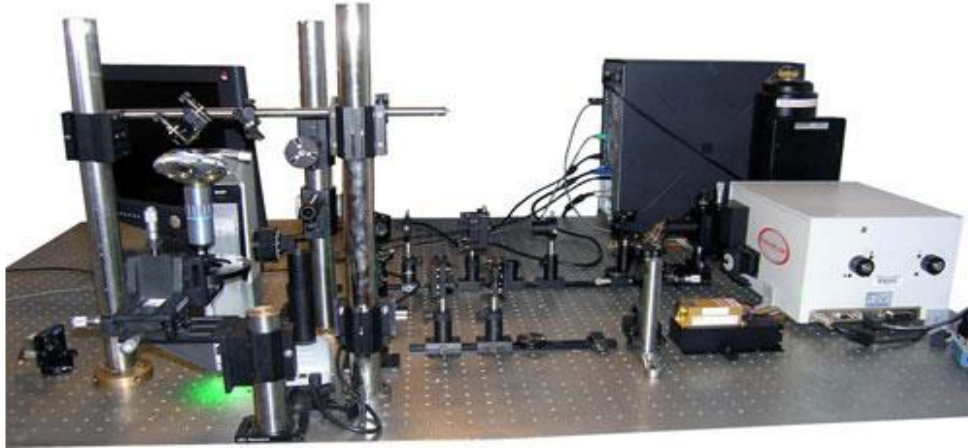

Figure 2.5 Raman Spectrometer (Courtesy: CSSS, ASU)

2.3.4 Rutherford Backscattering Spectrometry

The most common application of RBS is to investigate the composition, layered structure of thin films or bulks, on the other hand, RBS/channeling is a useful tool to provide the crystalline quality of the sample. The principles of RBS technique are billiard ball kinetics and energy loss. The high energy ion beam impinges onto the target, collides with the target atom and then gets backscattered into the detector which detects the yield and the kinetic energy of the backscattered ions.

In regular RBS, the energy of backscattering ions could be used to determine the layered structure of the thin films, while in RBS/channeling the yield of the backscattering ions indicates crystalline quality. In crystal, the atoms are arranged in an ordered pattern and can be treated as rows and planes[23]. Channeling happens in aligned direction in which the impinging ions are guided into the channels between rows and planes of atoms and pass through the channel. When ion channeling happens in crystalline materials, the backscattering yield from the bulk of the solid is reduced by two

orders of magnitude and a surface peak occurs at a position corresponding to scattering from the surface atoms[23]. So, the lower yield means better channeling, and better crystal quality.

Figure 2.6 shows how RBS works. A He^{2+} ion beam is generated at MeV energy by a General Ionex 1.7 MV tandem accelerator. The ions are dispersed by mass selection according to their mass, then the selected ions are bended in the magnets and guided to the beam line. In the beam line, the ions are collimated and focused. Eventually, the ion beam raster-scans over the specimen and backscattering ions are collected by a Si barrier detector. The energy and yield of the ions are converted to the voltage pulses and then amplified and sorted by the multichannel analyzer[24] .

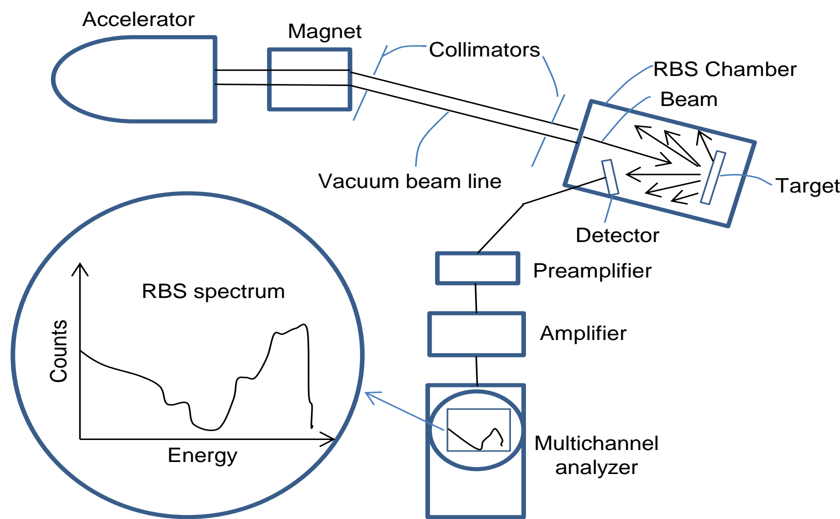

Figure 2.6 Schematic of a typical Rutherford backscattering Spectrometry instrumentation system[21]

The implantation damage before annealing and the extent of recrystallization in after annealing were investigated by preforming RBS/channeling on as-implanted samples and the annealed samples. The beam energy in RBS/channeling is 2MeV. The

backscattering yields in both random orientation and [001] channeled orientation are analyzed for each sample. The RBS spectrum was plotted by RUMP software.

2.3.5 Cross-section Transmission Electron Microscope

Transmission Electron Microscope is the expert in determining the microstructure of materials. In TEM, the electron beam is focused by several condenser lenses to form a nanometer spot size, which is the key to reveal the extremely small feature of the material[2]. The beam strikes the specimen which is thin enough that a portion of the beam is transmitted through the sample. The transmitted electrons are focused by objective lens into images and projected on fluorescent screen[2]. The other parts of the beam are diffracted.

The thickness of the sample should be specially prepared so that it allows the electron to transmit[2]. In our study, the samples for cross-section transmission electron microscopy (XTEM) analysis are prepared by Focused ion beam milling (FIB milling) using Nova 200 NanoLab focused ion beam tool. The surfaces of Si pieces were bonded together use the epoxy. Highly energetic gallium ion beam strikes the sample at a tilt angle and sputter the sample surface. The beam has sufficient energy to remove a portion of the sample and the beam spot is small enough to achieve a nanoscale specimen. The facility has an inbuilt scanning electron microscope to monitor the milling process in real time[25]. The equipment is also able to be programed to sputter out which part of the sample. Due to the high energy of the gallium ions, they will also be implanted into the top few nanometers of the surface, and sample surface will be amorphous.

The TEM micrographs provide information about morphology and defects in the specimen, so the cross-section transmission electron microscopy (XTEM) is performed on the as-implanted and annealed ion implanted samples to observe the evolution of defects and the recovery of the implantation damage during annealing.

2.3.6 Secondary Ion Mass Spectroscopy

Secondary Ion Mass Spectroscopy (SIMS) has been used extensively in depth profiling which gives the density of one element in the materials across the depth.

Sputtering is the basis of SIMS. Surface atoms in the sample are removed by their collisions with the incoming ions. During the collision, the keV primary ions having a relative low velocity interact with atom cores, experience nuclear energy loss and transfer their energy to the ejected surface atoms[4].

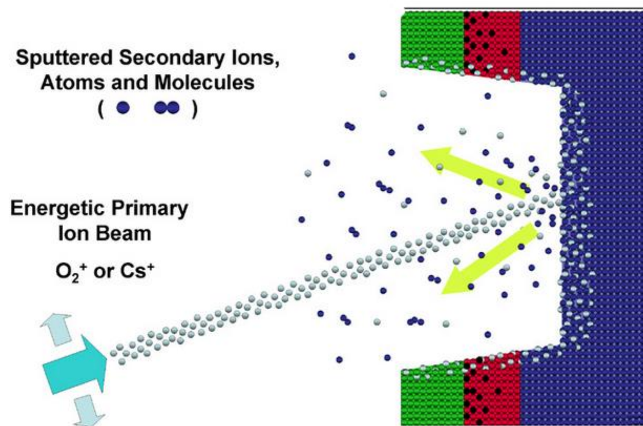

Figure 2.7 Schemitic of the working principle of SIMS[26]

Although most of the atoms and molecules are neutral when they are removed from the sample by the interaction between the primary beam and the sample surface, a

portion of them is ionized[27]. These ions are extracted by an electric field applied in the region between the sample and an extraction lens and accelerated in the presence of this field towards the magnetic sector analyzer which separates ions according to their mass to charge ratio. Then, the sorted ions are collected by faraday cup where the yield is counted. The emission of the secondary ions is monitored as a function of time, providing ion counts as a function of cycle time. By examining cycle time, one will have a general idea about the position of ions, but it doesn't give the direct information about depth. Generally, to convert cycle time and counts into the depth and concentration, the knowledge of sputtering rate and a calibration of the secondary ion signal are needed. Sputtering rate is calculated by measuring the crater depths of the sputtered sample, while calibration of the ion signal is done by using standards whose matrix and surface electronic properties match those of the specimen.

3 Results and discussion on the electrical and structural properties

3.1 Heating curves

When the microwave power is turned off, the temperature drops rapidly. The anneal time is defined as the time interval between the power on to power off. Figure 3.1 shows typical heating curves (anneal temperature as a function of time in the range of 200-1000 ^{o}C).

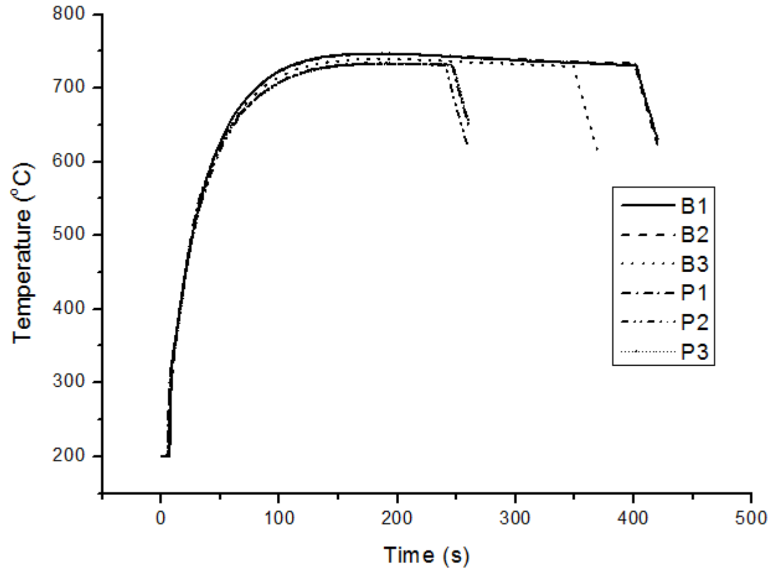

Figure 3.1 Temperature as a function of time measured by a pyrometer with a 200-1000 ^{o}C range for B^+ and P^+ implanted Si samples on SiC susceptor: (black dash) 2×10^{15} B^+ cm^{-2}, (red dash) 3×10^{15} B^+ cm^{-2}, (greed dash) 4×10^{15} B^+ cm^{-2}, (blue solid) 2×10^{15} P^+ cm^{-2}, (violet solid) 3×10^{15} P^+ cm^{-2}, (orange solid) 4×10^{15} P^+ cm^{-2}.

The maximum anneal times of B^+ implanted and P^+ implanted samples in our study are 400 s and 240 s, respectively. The temperature of B^+ implanted and P^+ samples reached the highest value at ~160 s and began to decrease slowly after ~ 230 s. The

highest temperature reached for all samples is on the order of ~ 740 ^{o}C. This suggests that dopant species and dose have little influence on the maximum microwave anneal temperature in amorphized Si when annealed with the assistance of a susceptor. Hence, the capability of microwave absorption in susceptor assisted microwave heating is more dependent on the bulk material (*i.e.,* Si) as opposed to a dependence on the presence of dopants.

3.2 Dopants electrical activation

During the microwave anneal, dopants move to substitutional positions and become electrically activated and this results in decreased R_{sh}. The drop of R_{sh} depends on the extent of dopant activation. The R_{sh} of the as-implanted samples is not measurable via four-point-probe analysis. Figure 3.2 shows the R_{sh} of B^+ and P^+ implanted samples as a function of different anneal times. The sheet resistances of P^+ implanted samples drops sharply within 40 s of annealing, and then remain constant, while R_{sh} of B^+ implanted samples decrease gradually and saturate at higher values within 200 s. Hall measurement results are tabulated in Table 1. The fraction of dopant activation is calculated by taking the ratio of sheet concentration (cm^{-2}) to the dose (ϕ). This fraction is ~ 16% for B^+ implanted Si, much lower than of the corresponding value for P^+ implanted Si, agreeing with the R_{sh} measurements. In other words, the P^+ implanted samples show more efficient electrical activation.

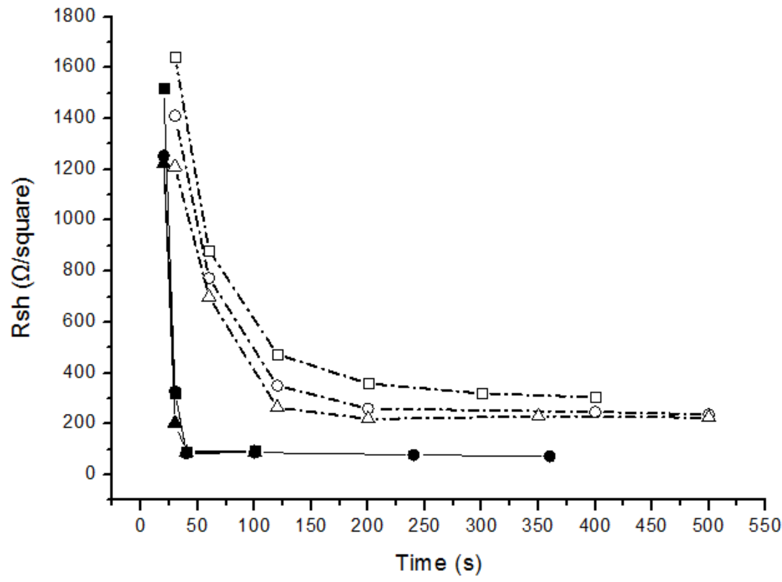

Figure 3.2 R_{sh} as function of time for P^+ and B^+ implanted Si wafers. (open square) 2×10^{15} B^+ cm^{-2}, (open circle) 3×10^{15} B^+ cm^{-2}, (open triangle) 4×10^{15} B^+ cm^{-2}, (solid square) 2×10^{15} P^+ cm^{-2}, (solid circle) 3×10^{15} P^+ cm^{-2}, (solid triangle orange solid) 4×10^{15} P^+ cm^{-2}

Table 1. Hall measurement results and activation calculation for 40s microwave annealed $2x10^{15}$ P^+ cm^{-2} and $4x10^{15}$ P^+ cm^{-2} implanted Si, 400s microwave annealed $2x10^{15}$ B^+ cm^{-2} implanted Si and 350s microwave anneal $4x10^{15}$ B^+ cm^{-2} implanted Si. The sheet thickness is approximated by 2Rp to obtain the sheet concentration.

Sample	Resistivity (Ω cm)	Carrier type	Sheet concentration (cm^{-2})	Bulk concentration (cm^{-3})	Mobility (cm^2/V-sec)	Fraction (%)
$2x10^{15}$ P^+ cm^{-2} backside	8.6	p	1.4×10^{14}	2.6×10^{15}	8.7	--
$2x10^{15}$ P^+ cm^{-2} front	95.1	n	1.3×10^{15}	2.7×10^{20}	51.3	64%
$4x10^{15}$ P^+ cm^{-2} front	83.1	n	1.6×10^{15}	3.5×10^{20}	46.1	41%
$4x10^{15}$ B^+ cm^{-2} backside	6.3	n	3.4×10^{13}	6.4×10^{14}	6.4	--
$4x10^{15}$ B^+ cm^{-2} front	219.7	p	6.0×10^{14}	5.1×10^{19}	47.2	15%
$2x10^{15}$ B^+ cm^{-2} front	313.6	p	3.6×10^{14}	3.1×10^{19}	55.6	18%

The regrowth rate of the amorphous layer during solid phase epitaxial growth affects the efficiency of electrical activation significantly[28]. After the initial 30 s anneal, the R_{sh} of P^+ implanted Si is lower than that of B^+ implanted Si. The relatively high effective carrier concentration in P^+ implanted Si enables its amorphous layer to regrow

faster [28]. Since the regrowth rate and the electrical activity of the layer near the amorphous-crystalline interface are closely interrelated[28], the faster regrowth rate in P^+ implanted sample in turn enhances the its electrical activation. This positive feedback enables its recrystallization and electrical activation to occur in a much shorter time of 40 s, compare to the B^+ implanted Si

3.3 Recrystallization and defects evolution

Besides electrical activation, ion implantation damages are removed and Si wafer is recrystallized by annealing. Basically, the amorphous layer and crystalline silicon can be differentiated by the Raman Spectra due to their characteristic molecular vibration. The crystalline quality could be accessed by backscattering yield in RBS/ion channeling. The lower the backscattering yield in the spectra, the better the crystalline quality of the sample. Finally, TEM could show the micrographs of amorphous and crystalline structure and defects directly.

3.3.1 Raman Spectra

Figure 3.3 displays Raman spectra from as-implanted and annealed samples. In the Raman spectra of the P^+ implanted samples shown in Figure 3.3(a), the as-implanted and 20 s annealed samples each have a broad peak at 470-480 cm^{-1} and this corresponds to the amorphous Si layer created by implantation. The sharp peak at 520 cm^{-1} in the as-implanted sample is from the crystalline Si in the substrate[29] ; while, the sharp crystalline

Si peak at 520 cm^{-1} in 20 s annealed sample is attributed to both Si substrate and partially crystallized Si surface. The penetration depth of the laser used in Raman Spectroscopy extends beyond the amorphous layer and into the crystalline Si (c-Si) substrate, resulting in Si substrate contributing to the Si Raman line [30]. After a 40 s anneal, the broad amorphous Si (a-Si) peak disappears and the magnitude of the 520 cm^{-1} crystalline Si peak increases. This indicates that more crystalline Si has formed in the sample compared to the 20 s anneal. Even with a 100 s anneal, the magnitude of crystalline Si peak does not increase further, which means that the damaged Si lattice has been repaired entirely after 40s. It should be noted that the crystalline Si peaks in these samples originate from both the c-Si substrate and the recrystallized Si near the surface. Hence, the FWHM (full width at half maximum) of the peaks, which is an indication of the crystalline quality of the materials cannot be used on its own to determine the quality of our samples[31].

In the Raman spectra from the B^+ implanted samples, shown in Figure 3.3(b), the 520 cm^{-1} single-crystal Si peaks from the 200 s and 350 s annealed samples overlap, indicating that recrystallization of the amorphous Si layer is complete after 200 s. The amorphous Si peak in the B^+ as-implanted sample is not as pronounced as that of the P^+ implanted sample, but the broad shoulder at 480 cm^{-1} indicates that the sample still contains a small amount of amorphous Si. Moreover, the single-crystal Si peak in the B^+ as-implanted sample is very strong and is comparable to the corresponding peak of the annealed samples, indicating that the amount of damage in the B^+ as-implanted sample is small compared to the P^+ implanted sample. Since the implantation energy of the boron falls into the energy range where electronic energy losses dominate over nuclear energy losses, the boron ions primarily experience electronic energy losses which cause lower

amounts of damage[4]. It is also visible in Figure 3.3 that the Si peak tails are enhanced on the high-energy side of the peaks. Such asymmetric Raman lines are due to the Fano effect caused by the high dopant concentrations[32].

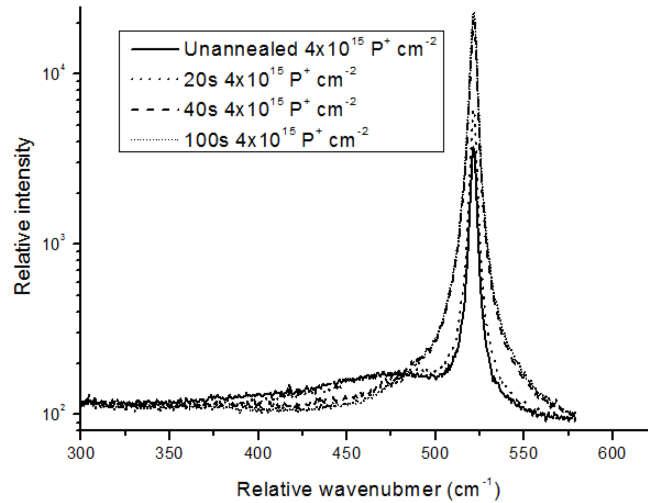

(a)

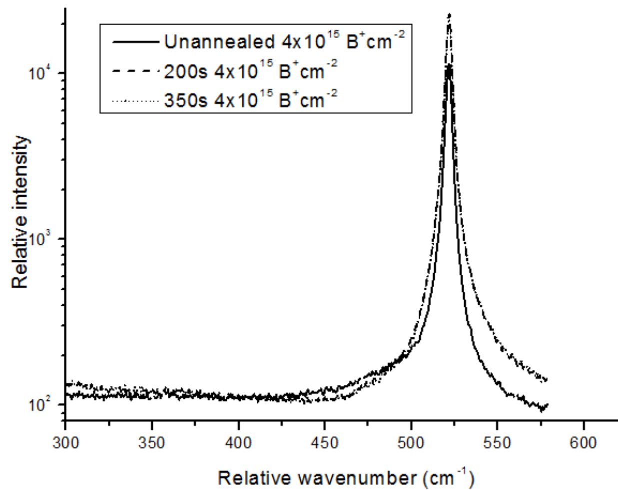

(b)

Figure 3.3 Raman Spectra from ion implanted Si: (a) 4×1015 P+ cm-2 with different anneal times; (b) 4×1015 B+ cm-2 with different anneal times

3.3.2 RBS/ion channeling spectra

RBS spectra from 4×10^{15} P^+ cm^{-2} implanted Si and 2×10^{15} B^+ cm^{-2} implanted Si prior to and after annealing, obtained in random and [001] channeling directions, are shown in Figure 3.4. The lower the backscattering yield in the spectra, the better the crystalline quality of the samples. The crystalline quality of the annealed samples is accessed by calculating χ_{min}, the ratio of the minimum yield in the aligned spectrum to the yield in the random spectrum. The χ_{min} values for P^+ implanted and B^+ implanted Si is 5.1% and 10.3%, respectively. These values indicate that both sets of samples have achieved good crystalline quality, with the P^+ implanted Si showing a slightly better quality. In comparison, unimplanted Si shows χ_{min} of 4% [12].

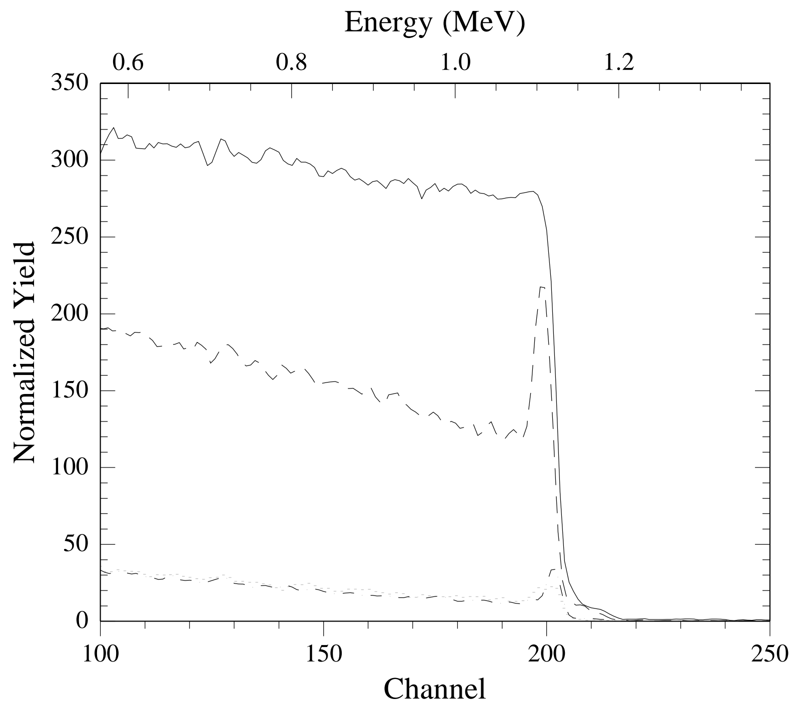

(a)

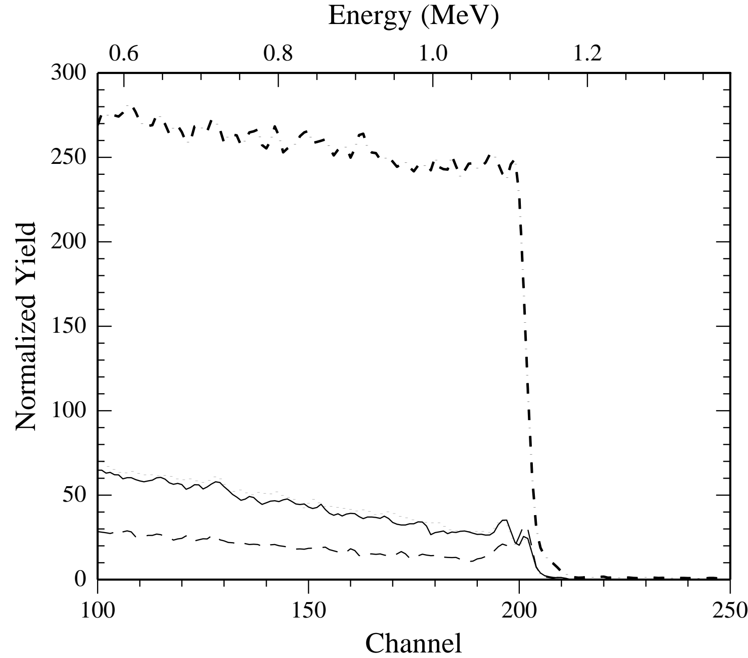

(b)

Figure 3.4 RBS spectra from ion implanted Si samples. (a) ion channeling of 4×10^{15} P^+ cm^{-2} implanted Si: as-implanted in a random direction (solid line), as-implanted in [001] direction (dash line), annealed for 40 s in a [001] direction (dash-dot line), annealed for 100 s in [001] direction (dot line). (b) ion channeling of 2×10^{15} B^+ cm^{-2} implanted Si: as-implanted in random direction (dash-dot line), as-implanted in [001] direction (dash line), annealed for 200 s in [001] direction (solid line), annealed for 400 s in [001] direction (dot line).

RBS spectra from P^+ annealed samples (Figure 3.4(a)) show lower backscattering yield when compared to the yield of the as-implanted samples. Ion channeling from the 40 s and 100 s annealed samples produce similar spectra, indicating that repair of implant damage in the Si layer is completed after 40 s. This finding is consistant with the Raman results. In Figure 3.4(b), the backscattering yield in the channeling direction for the B^+ as-implanted samples is anomalously low compared to the value for the annealed samples. In addition, an anomalous surface peak is present next to the outermost surface peak in this ion channeling spectrum and its height increases upon annealing. These observations

suggest that extended defects such as dislocation loops that form under the Si surface during annealing leading to the second surface peak. The defects cause de-channeling of the incident RBS ions, eventually resulting in increased backscattering yield from the annealed sample[23].

3.3.3 TEM images

TEM was performed to check defects under the surface of the B^+ implanted Si, and the resulting TEM micrographs are shown in Figure 3.5. In Figure 3.5(a), the black dots at the c-Si to a-Si interface, in the as-implanted Si, are Si interstitial clusters resulting from coalescence of Si interstitials that are created by the implantation[1,33]. With a 200 s anneal, the Si interstitial clusters grow into dislocation loops as shown in Figure 3.5(b). These defects lead to de-channeling of the RBS ions, which explains the anomalous backscattering yield observed in the case of the annealed samples. After an additional 200 s anneal at the same temperature of 747 ^{o}C, the small dislocation loops dissolve by emitting Si interstitials. The emitted Si interstitials are transported to larger dislocation loops resulting in Ostwald ripening of the loops. This mechanism then causes an increase in size and a decrease in density of the dislocation loops as seen in Figure 3.5(c) compared with Figure 3.5(b)[34].

The as-implanted Si has an amorphous layer on the surface, which is visible as a thick white layer at the top of the Si sample in Figure 3.5(a). After microwave annealing, the amorphous layer has recrystallized as can be seen in Figure 3.5(b) and Figure 3.5(c). Even though the as-implanted Si contains an amorphous top layer and this layer has

recrystallized in the annealed samples, the as-implanted Si still has the lowest backscattering yield in the RBS ion channeling spectrum because defects in the annealed samples cause more severe de-channeling.

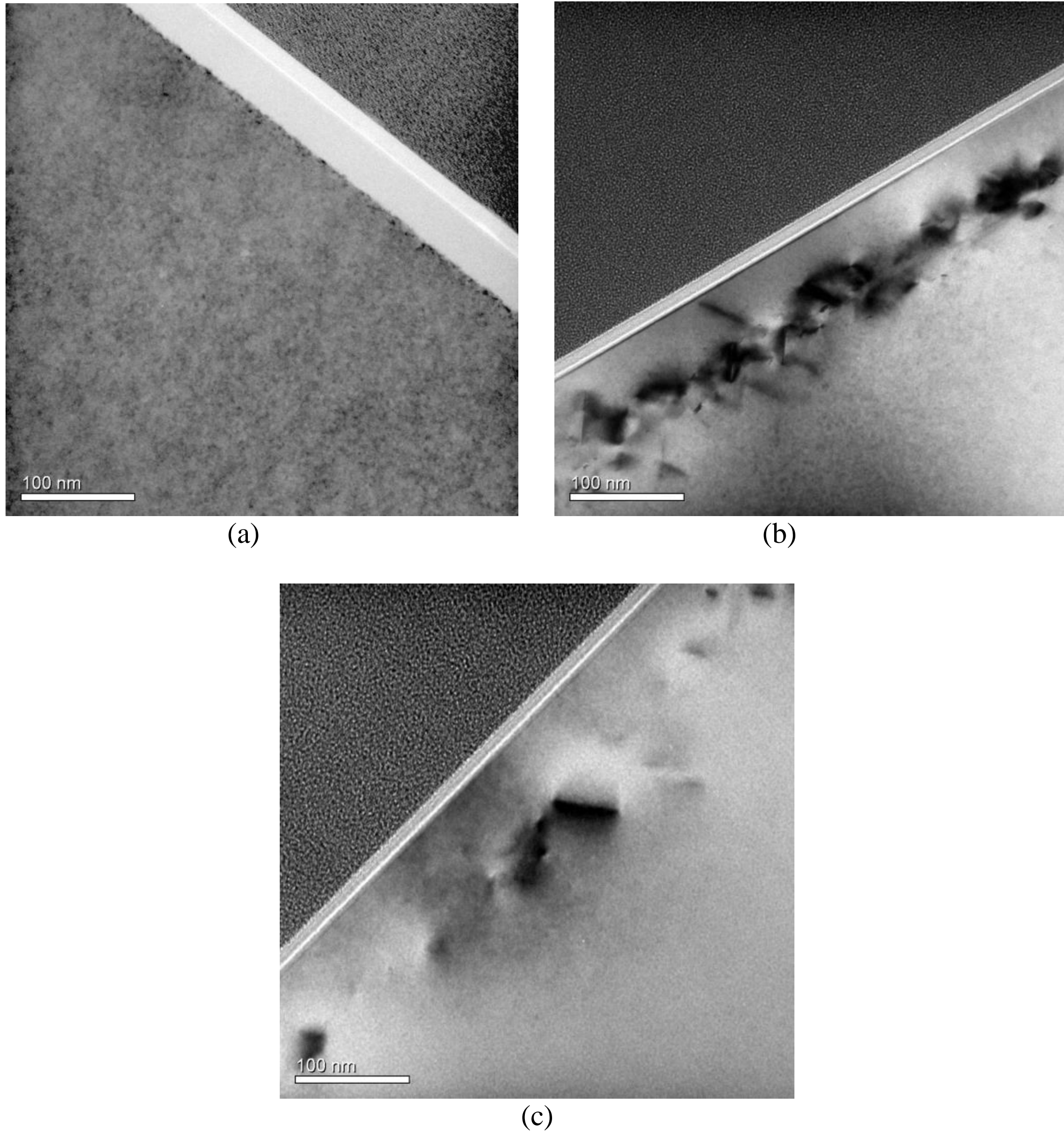

(a) (b)

(c)

Figure 3.5 TEM micrographs from 2×10^{15} B^+ cm^{-2} implanted Si (a) as-implanted; (b) after microwave 200s annealing; (c) after 400s annealing.

3.3.4 SIMS profiles

Figure 6 shows SIMS profiles of 4×10^{15} B^+ implanted Si and 2×10^{15} P^+ implanted Si prior to and after annealing. The boron profiles after microwave annealing for 200 s and 350 s, where the peak temperature reaches 747 °C (Figure 3.6 (a)), show immobile boron peaks and extended tails that are typical characteristics of transient enhanced diffusion (TED). Such transient enhanced diffusion is a common occurrence in boron implanted silicon[35,36,37].

The immobile peaks are associated with extended defects which trap the boron dopants, as well as the formation of boron-silicon interstitial complexes (BICs) that are immobile and impede dopant activation[38]. The presence of dislocation loops in TEM micrographs of the 200 s annealed 2×10^{15} B^+ implanted Si (Figure 5(b)) is consistent with this explanation. The extended tail region is due to TED in the course of which Si self-interstitials kick-out substitutional boron atoms leading to mobile boron interstitials, or form mobile Si-B pairs that can diffuse [34,36,37].

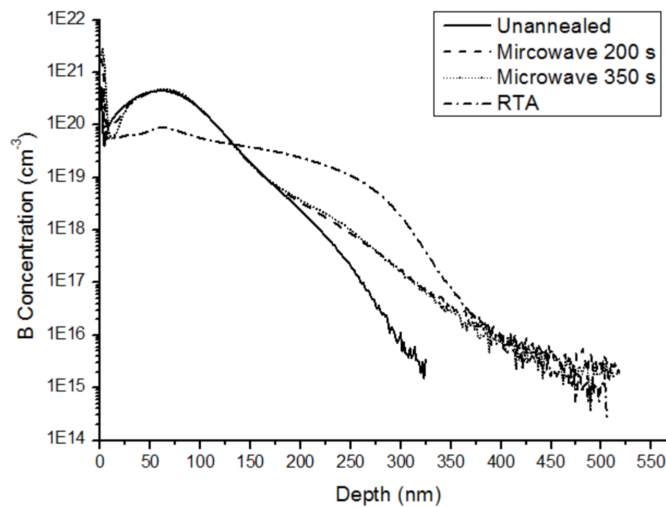

(a)

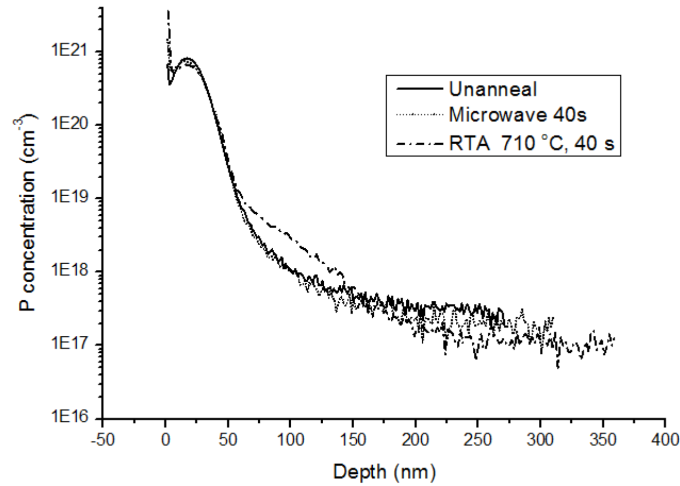

(b)

Figure 3.6 SIMS profile from ion implanted Si prior to and after annealing. (a) 4×10^{15} B^+ cm^{-2} implanted Si with microwave annealing for 200 s and 350 s as well as RTA for 90 s at 950 ^oC (b) 2×10^{15} P^+ cm^{-2} implanted Si with microwave annealing for 40 s and RTA for 40 s at 710 ^oC.

The boron profiles from the 200 s and 350 s microwave annealed samples overlap in Figure 6(a), which means that no further diffusion occurs after 200 s of annealing. This absence of further diffusion is due to the strong dependence of TED on the supersaturation of free Si interstitials[36,37]. During the initial stages of annealing, small interstitial clusters are not stable, and they tend to grow by consuming free Si self-interstitials; this results in the decay of the supersaturation of free Si interstitials. During this stage, the supersaturation of Si interstitials is still enough to cause TED but with a gradually decreasing rate[36]. In the later stages, due to Ostwald ripening, large dislocation loops grow in size by capturing the emitted the Si atoms from small dislocation loops. The small dislocation loops dissolve and finally disappear. Compared to the early stage, the supersaturation of Si interstitials at this stage is much lower[36], and so TED almost stops, which explains why no diffusion happens after 200 s annealing.

Consider the boron profile of the RTA sample (950 ^{o}C for 90 s) in Figure 3.6(a). The significant boron diffusion observed in the profile is likely due to a large amount of Si interstitials and boron dopants which are released during the dissolution of extended defects in the sample [35,36, 38]. The high temperature of the anneal is likely to remove most dislocations and BICs [36,38], leaving behind a supersaturation of free Si interstitials and extensive boron dopants which cause the severe diffusion[35,38].

This scenario is supported by the sheet resistance values of the RTA samples. To a certain extent, the sheet resistance can reflect the crystalline quality of the samples, since increased dislocations are likely to getter dopant atoms and therefore reduce the total activated dopants. The fact that the sheet resistance of the RTA sample is 43 Ω/square, much lower than the 230 Ω/square measured from the 350 s microwave annealed sample, suggests that the RTA sample has better crystalline quality and fewer dislocations.

In terms of comparing RTA and microwave annealing for P^+ implanted Si, RTA and microwave annealing were first done in similar conditions, including same peak temperature of 584 ^{o}C, and similar dwell time but different total anneal time, which are listed in Table 2. The sheet resistance of RTA treated P^+ implanted Si is much higher than that of microwave annealed Si sample. Hence, under similar condition, microwave annealing can achieve a better electrical activation than RTA when annealing P^+ implanted Si.

Table 2 The condition of microwave annealing and RTA in P+ implanted Si wafers and the corresponding sheet resistance.

Annealing condition	Microwave 40 s	RTA 584°C	RTA 710°C
Total time	40 s	30 s	74 s
Ramp time	40 s	29 s	34 s
Peak Temperature and dwell time	584°C, 0 s	584°C, 1 s	710°C, 40 s
R_{sh} (Ω/square)	88	144	88

Then, to ensure the RTA and microwave annealing achieve the same sheet resistance in P^+ implanted Si, RTA and microwave annealing were done in different conditions which are listed in Table 2, resulting the same sheet resistances of 88 Ω/square. The condition of microwave annealing was fixed, which still has a total time of 40 s and peak temperature of 584 ^oC, while RTA was done with a peak temperature of 710 ^oC and 74 s total anneal time. Then the diffusions of dopants were compared using samples having the same electron acitvation. A SIMS profile obtained from P^+ implanted Si with the same sheet resistance is shown in Figure 3.6(b). Nearly no phosphorus diffusion happens after 40s microwave annealing, but phosphorus diffusion is obvious in the sample annealed with RTA at 710 ^oC for 40 s. Considering the electrical activation and diffusion, microwave annealing for P^+ implanted Si can achieve better result than RTA in the low temperature annealing.

4 Discussion on the heating behavior

According to the microwave heating mechanism, ion implanted Si interacts with the microwave and generate heat by the conduction losses and polarization losses[14]. However, ion implanted Si is heat to a relatively low temperature by absorbing microwave only[11]. To achieve a temperature that is high enough to repair the damages and activate the dopants, assisted mechanism is required. We use SiC susceptor to provide conductive heating to ion implanted samples, assisting the samples in ramping up to high temperature. In our study, the heating of ion implanted sample is attributed to both microwave absorption of the sample itself and the thermal conduction from the SiC-Al_2O_3 susceptor.

The main contributor to the heating of the Si was evaluated by comparing the heating curve of ion-implanted Si-on-susceptor with the heating curve of the SiC susceptor alone in Figure 4.1. The data in the figure indicates that in the first 20 s to reach 455 ^{o}C, the temperature of the ion implanted Si sample is higher than that of the susceptor. Therefore thermal conduction will occur from the Si which is at a higher temperature to the susceptor which is at a lower temperature. This means that the susceptor does not supply any additional heat to the Si samples. Hence, Si self-heating by microwave absorption is the main contributor to the heating of the Si sample.

After ~ 20 s at 455 ^{o}C, the temperature of the susceptor is higher than that of the Si on the susceptor. Hence, there now is thermal conduction from the SiC susceptor to the Si and this helps heat the Si. Meanwhile the Si sample also absorbs microwave power. So, after ~20 s, Si self-heating and conductive heating contribute to the heating of Si together.

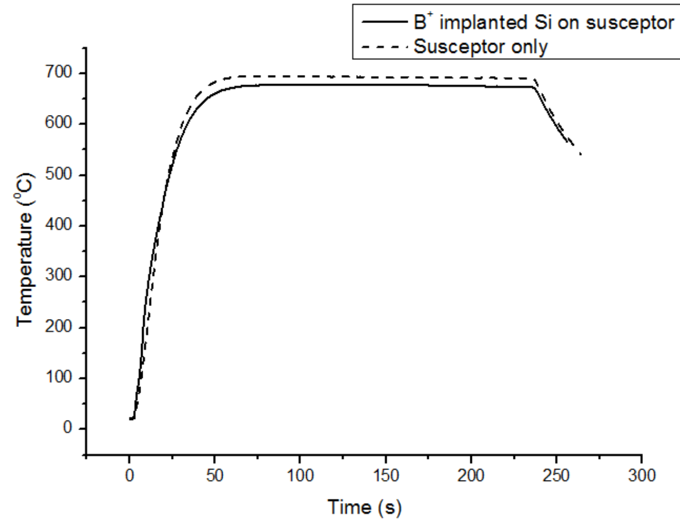

Figure 4.1 The temperature as a function of time for SiC susceptor alone and 2×10^{15} B^{+} cm^{-2} implanted Si on susceptor.

5 Summary and Conclusion

Driven by the International Technology Roadmap for Semiconductors (ITRS), the device features are scaling down significantly and the corresponding junction depth keeps decreasing[12]. However, the most widely used technique, rapid thermal annealing, still cannot minimize the diffusion length sufficiently[10]. Several other thermal annealing techniques, such as laser annealing and metal induced crystallization suffer from either non-uniform heating or metal contamination[6-9]. Fortunately, it is reported that susceptor-assisted microwave annealing only leads to a limited diffusion[10]. To achieve a shallow junction, a low energy of 15 keV is applied in the boron and phosphorus implantation and the susceptor-assisted microwave annealing is conducted to minimize the diffusion in this study.

The electrical and structural properties of B^+ implanted and P^+ implanted Si samples before and after microwave annealing are investigated. The results of this study confirm that microwave annealing is able to achieve sufficient recrystallization and electrical activation. The low implantation-energy used in this study, creates lower amount of damage in B^+ implanted Si, compared with P^+ implanted Si. However, annealing induces the growth of large extended defects and results in reduced crystalline quality and impeded the electrical activation in the B^+ implanted Si. The P^+ implanted sample on the other hand experiences more effective electrical activation and better crystalline quality after annealing. Dopant diffusion in the microwave annealed B^+ implanted samples is not as severe as in the RTA processed sample because BICs in the microwave annealed sample confine Si interstitials and thereby minimize diffusion of the

boron dopant atoms. The annealed P^+ implanted Si shows no measureable diffusion after the microwave-induced crystallization and electrical activation is completed. During susceptor-assisted microwave annealing, Si self-heating by microwave absorption is the main contributor to the temperature rise of Si in the first 20 s. After 20 s annealing, the conductive heating from SiC susceptor also participates in the heating of Si. The extent of microwave absorption in susceptor-assisted microwave heating depends on the bulk materials being heated, rather than the implanted dopant species and dose.

6 Further work

Although we have successful minimized the dopants diffusion using a fast annealing technique, susceptor-assisted microwave annealing, severe defects in boron implanted Si wafers might have bad influence on the transistors' performance if these defects are electrically active. For example, the electrically active defects are deep level traps where the electrons and holes in the wafer would be captured and emitted and then cause the leakage and degraded performance in the transistors. Hence, one of the further work is to determine whether those defects are electrically active or not.

Secondly, we want to find out the quantitative dependence of the dielectric loss on temperature in lower temperature range. Hence, in the further, the dielectric loss would be measured as a function of temperature using electromagnetic measurement method.

REFERENCES

1 Wolf, S. and Tauber, R. N., *Sillcion Processing For The VLSI Era, VOLUME 1: PROCESSING TECHNOLOGY* (California: Lattice Press, 1986).

2 Alford, T. L., L. C. Feldman, and J.W. Mayer, *Fundamentals of Nanoscale Film Analysis* (New York: Springe, 2007).

3 D. K. Schroder, *Semiconductor Material and Device Characterization* (Hoboken: Wiley, 2006).

4 J. W. Mayer and S. S. Lau, *Electronic Materials Science: For Integrated Circuits in Si and GaAs* (New York: Macmillan, 1990).

5 S. Mahajan and K.S. Sree Harsha, *Principles of growth and processing of semiconductors* (New York: McGraw-Hill, 1999).

6 J. Krynicki, J. Suski, S. Ugniewski, R. Grötzschel, R. Klabes, U. Kreissig, J. Rüdiger, “Laser annealing of arsenic implanted silicon”, *Physics Letters A* 61 (1977): 181-182.

7 P. Baeri, S.U. Campisano, G. Foti, E. Rimini, “A melting model for pulsing-laser annealing of implanted semiconductors”, *Journal of Applied Physics* 50 (1979): 788-797.

8 T. J. Konno and R. Sinclair, “Metal-contact-induced crystallization of semiconductors”, *Materials Science and Engineering: A* 179 (1994): 426-432.

9 L. Hultman, A. Robertsson, H. T G Hentzell, I. Engstrom and P. A.Psaras, "Crystallization of amorphous silicon during thin film gold reaction", *Journal of Applied Physics* 62 (1987): 3647-3655.

10 R. N. Vemuri, M. J. Gadre, N. D. Theodore, W. Chen, S.S. Lau and T. L. Aflord, “Susceptor assisted microwave annealing for recrystallization and dopant activation of arsenic-implanted silicon”, *Journal of Applied Physics* 110 (2011): 034907.

11 T.E. Seidel, D.J. Lischner, C.S. Pai, R.V. Knoell, D.M. Maher and D.C. Jacobson, “A review of rapid thermal annealing (RTA) of B, BF2 and As ions implanted into silicon”, *Nuclear Instruments and Methods in Physics Research Section B* 7–8 (1985): 251-260.

12 Alford, T. L., D. C. Thompson, J. W. Mayer, and N. David Theodore. “Dopant activation in ion implanted silicon by microwave annealing.” *Journal of Applied Physics* 106, no. 11 (2009): 114902-114902.

13 Clark, D. E. and W. H. Sutton, “Microwave Processing of Materials”, *Annu. Rev. Mater. Sci.* 26 (1996): 299-331.

14 Hummel, R. E., *Electric Properties of Materials* (New York: Springer, 2011).

15 Meredith, R., *Engineers’ Handbook of Industrial Microwave Heating*, (London: The Institution of Electrical Engineers, 1998).

16 Thostenson, E.T., T.W. Chou, “Microwave processing: fundamentals and applications”, *Composites Part A: Appl. Sci. and Manufacturing* 30 (1999): 1055-1071.

17 Metaxas, A. C. and R.J. Meredith, *Industrial Microwave Heating* (London: Peter Peregrinis, 1983).

18 Grant, E. H, and BenáS J. Halstead. “Dielectric parameters relevant to microwave dielectric heating.” *Chemical Society Reviews* 27, no. 3 (1998): 213-224.

19 Damm, M., and C. Oliver Kappe. "Parallel microwave chemistry in silicon carbide reactor platforms: an in-depth investigation into heating characteristics." *Molecular diversity* 13, no. 4 (2009): 529-543.

20 Vemuri, R. "Susceptor assisted microwave annealing of ion implanted silicon." PhD diss., Arizona State University, 2011.

21 Crankovic, G. M. *ASM Handbook, Volume 10:.: Materials Characterization*. ASM International, 1986.

22 Poweleit, C. D., A. Gunther, S. Goodnick, and José Menéndez. "Raman imaging of patterned silicon using a solid immersion lens." *Applied physics letters* 73 (1998): 2275-2277.

23 Feldman, L.C., J. W. Mayer and S. T. Picraux, *Materials Analysis by Ion Channeling: submicron crystallography*, (New York : Academic Press, 1982).

24 Chu, Wei-Kan, James W. Mayer, and Marc-A. Nicolet. *Backscattering spectrometry*. (New York: Academic Press, 1978).

25 Giannuzzi, Lucille A., B. W. Kempshall, S. M. Schwarz, J. K. Lomness, B. I. Prenitzer, and F. A. Stevie. *FIB lift-out specimen preparation techniques*. (New York: Springer, 2005).

26 http://researcher.watson.ibm.com/researcher/view_project_subpage.php?id=3575

27 Escobar Galindo, R., R. Gago, J. M. Albella, and A. Lousa. “Comparative depth-profiling analysis of nanometer-metal multilayers by ion-probing techniques.” *TrAC Trends in Analytical Chemistry* 28, no. 4 (2009): 494-505.

28 Suni, I., G. Göltz, M-A. Nicolet, and S. S. Lau. “Effects of electrically active impurities on the epitaxial regrowth rate of amorphized silicon and germanium.” *Thin Solid Films* 93 (1982): 171-178.

29 Fong, S. C., C. Y. Wang, T. H. Chang, and T. S. Chin. “Crystallization of amorphous Si film by microwave annealing with SiC susceptors.” *Applied Physics Letters* 94, no. 10 (2009): 102104-102104

30 http://www.srim.org/

31 Boultadakis, S., S. Logothetidis, and S. Ves. “Comparative study of thin poly - Si films grown by ion implantation and annealing with spectroscopic ellipsometry, Raman spectroscopy, and electron microscopy.” *Journal of applied physics* 72, (1992): 3648-3658.

32 Nickel, N. H., P. Lengsfeld, and I. Sieber. "Raman spectroscopy of heavily doped polycrystalline silicon thin films." *Physical Review B* 61 (2000): 15558.

33 Plummer, James D. *Silicon VLSI technology: fundamentals, practice, and modeling*. (India: Pearson Education, 2009).

34 Calvo, P., A. Claverie, N. Cherkashin, B. Colombeau, Y. Lamrani, B. De Mauduit, and F. Cristiano. “Thermal evolution of {113} defects in silicon: transformation against dissolution.” *Nuclear Instruments and Methods in Physics Research Section B: Beam Interactions with Materials and Atoms* 216 (2004): 173-177

35 Michel, A. E., W. Rausch, P. A. Ronsheim, and R. H. Kastl. "Rapid annealing and the anomalous diffusion of ion implanted boron into silicon." *Applied physics letters* 50 (1987): 416-418.

36 Jain, S. C., Wim Schoenmaker, Richard Lindsay, P. A. Stolk, Stefaan Decoutere, Magnus Willander, and H. E. Maes. “Transient enhanced diffusion of boron in Si.” *Journal of applied physics* 91 (2002): 8919-8941.

37 Claverie, A., L. F. Giles, M. Omri, B. De Mauduit, G. Ben Assayag, and D. Mathiot. “Nucleation, growth and dissolution of extended defects in implanted Si: impact on dopant diffusion.” *Nuclear Instruments and Methods in Physics Research Section B: Beam Interactions with Materials and Atoms* 147 (1999): 1-12

38 Cristiano, F., X. Hebras, N. Cherkashin, A. Claverie, W. Lerch, and S. Paul. "Clusters formation in ultralow-energy high-dose boron-implanted silicon." *Applied physics letters* 83 (2003): 5407-5409